


RESEARCH

Open Access



# Permeability anisotropy in sandstones from the Soultz-sous-Forêts geothermal reservoir (France): implications for large-scale fluid flow modelling

Margaux Goupil<sup>1\*</sup>, Michael J. Heap<sup>1,2\*</sup>  and Patrick Baud<sup>1</sup>

\*Correspondence:  
margaux.goupil@etu.unistra.fr;  
heap@unistra.fr

<sup>1</sup> Université de Strasbourg, CNRS, Institut Terre et Environnement de Strasbourg, UMR 7063, 5 Rue Descartes, 67084 Strasbourg, France

<sup>2</sup> Institut Universitaire de France (IUF), Paris, France

## Abstract

The successful exploitation of geothermal reservoirs relies upon the understanding of fluid circulation in the subsurface. However, large-scale fluid flow modelling often assumes that the permeability of the layers of rock within the model are isotropic. We present here a laboratory study in which we assessed the permeability anisotropy of seven Buntsandstein sandstone cores taken from the geothermal reservoir at Soultz-sous-Forêts (France) in the Upper Rhine Graben. The porosity and permeability of our samples, cored parallel and perpendicular to bedding, ranged from 5.2 to 16.3% and from  $2.48 \times 10^{-18}$  to  $7.66 \times 10^{-14}$  m<sup>2</sup>, respectively. Our data show that permeability anisotropy can be up to four orders of magnitude in sandstones from the Buntsandstein, and that permeability anisotropy increases as a function of increasing porosity. Quantitative microstructural analysis combined with permeability modelling shows that the permeability anisotropy is the result of fine-grained and low-permeability laminations that are parallel or sub-parallel to bedding. We suggest, based on our data, that permeability anisotropy should be considered in future fluid flow modelling at geothermal sites within the Upper Rhine Graben.

**Keywords:** Buntsandstein, P-wave velocity, Porosity, Grain size distribution

## Introduction

Due to the current global climate crisis, geothermal exploitation is becoming increasingly relevant. To optimise the productivity of geothermal reservoirs, understanding fluid circulation in the subsurface is essential (Huenges and Ledru 2011). The permeability, i.e. the capacity for fluid to pass through a porous or granular medium (Guéguen and Palciauskas 1994), of rock is one of the key factors that controls fluid flow in the Earth's upper crust, and is therefore an important input parameter in large-scale models designed to better understand fluid circulation within geothermal reservoirs (Hicks et al. 1996; Guillou-Frottier et al. 2013; Magnenet et al. 2014; Vallier et al. 2018, 2019; Duwiquet et al. 2019, 2021).

The Upper Rhine Graben, part of the European Cenozoic Rift System, has been exploited for geothermal energy for decades (Vidal and Genter 2018; Glaas et al. 2021) owing to the presence of thermal anomalies (Pribnow and Schellschmidt 2000; Baillieux et al. 2013). The geology of the area consists of a fractured granitic basement (Genter and Traineau 1996; Dezayes et al. 2010, 2021; Ledésert et al. 2010; Villeneuve et al. 2018), overlain by Permo-Triassic (Buntsandstein, Muschelkalk, and Keuper; Haffen et al. 2013; Vidal et al. 2015; Aichholzer et al. 2016, 2019; Heap et al. 2017, 2018, 2019a; b; Kushnir et al. 2018a, b; Harlé et al. 2019) and Jurassic (Lias and Dogger) sedimentary rocks (mainly sandstones and carbonate rocks) and more-recent sedimentary rocks and sediments (Aichholzer et al. 2016; Düringer et al. 2019). The Buntsandstein, a ~1-km-thick succession of sandstones which directly overlies the granitic basement (Aichholzer et al. 2016; Düringer et al. 2019), forms the top of the regional convection zone (Vidal et al. 2015) and is therefore important for large-scale fluid flow and convection.

Large-scale modelling has sought to better understand regional fluid flow and convection at various geothermal sites within the Upper Rhine Graben (Guillou-Frottier et al. 2013; Magnenet et al. 2014; Vallier et al. 2018, 2019). For example, Magnenet et al. (2014) showed, using a thermo-hydro-mechanical model, that > 1 km convection cells at Soultz-sous-Forêts (France) require a permeability of  $10^{-14}$  m<sup>2</sup>. Using a similar model, Vallier et al. (2018) suggested that the lithological transition at Soultz-sous-Forêts between the sediments and the granitic basement does not significantly influence hydrothermal circulation. Modelling at a nearby geothermal site, Rittershoffen (France), highlighted similarities between the rock properties at Rittershoffen and Soultz-sous-Forêts (Vallier et al. 2019). As outlined in Guillou-Frottier et al. (2013) and Magnenet et al. (2014), the value or values of permeability used in such models can have a considerable impact on convective patterns, which can influence decisions about the position of future sites of geothermal exploitation. Therefore, it is crucial for geothermal energy exploitation that large-scale fluid flow models are as accurate as possible.

Although we have learnt a lot from previous studies, a commonality of large-scale fluid flow modelling designed to understand hydrothermal convection in geothermal reservoirs is that the permeability of the different layers within the model is often assumed to be isotropic. However, sedimentary rocks such as sandstones are often anisotropic in terms of their strength (Baud et al. 2005; Louis et al. 2005, 2009; Kim et al. 2016) and their permeability (Benson et al. 2003, 2005; Clavaud et al. 2008; Dautriat et al. 2009; Baud et al. 2012; Gehne and Benson 2017; Meng et al. 2021). These studies, and others, have shown that the permeability of sandstone parallel to bedding can be higher than the permeability perpendicular to bedding, and that this is due to a pore shape preferred orientation and/or bedding-parallel, low-permeability layers. For example, Clavaud et al. (2008) found that the permeability anisotropy ratio ( $k_{\text{perp}}/k_{\text{para}}$ ; where  $k_{\text{perp}}$  and  $k_{\text{para}}$  are the permeabilities perpendicular and parallel to bedding, respectively) of a suite of sandstones (porosities = 12–25%) were 0.19–0.77. Permeability anisotropy ratios were measured to be ~0.44, ~0.64, ~0.23, and ~0.75 for Crab Orchard sandstone (porosity = 5%; Benson et al. (2003, 2005)), Diemelstadt sandstone (porosity = 23%; Baud et al. (2012)), Rothbach sandstone (porosity = 24%; Meng et al. (2021)), and Adamswiller sandstone (porosity = 26%; Meng et al. (2021)), respectively. Benson et al. (2005) and Gehne and Benson (2017) also showed that the permeability anisotropy of Crab Orchard sandstone

decreased as a function of increasing effective pressure; however, Baud et al. (2012) and Meng et al. (2021) found that the permeability anisotropies of Diemelstadt, Rothbach, and Adamswiller sandstones were not influenced by effective pressure. Not only is the matrix permeability of sandstones typically anisotropic, but also the permeability, and permeability anisotropy, of sandstone can be further complicated by the presence of meso- and macroscale fractures that can act as barriers to or conduits for fluid flow (Zhu and Wong 1997; Shipton et al. 2002; Farrell et al. 2014, 2021; Griffiths et al. 2016; Farrell and Healy 2017; Kushnir et al. 2018b).

To help large-scale fluid flow modelling in the Upper Rhine Graben, we present here a study in which we quantified the permeability anisotropy of reservoir sandstones (from the Buntsandstein) taken from exploration well EPS-1 at Sultz-sous-Forêts (Fig. 1).

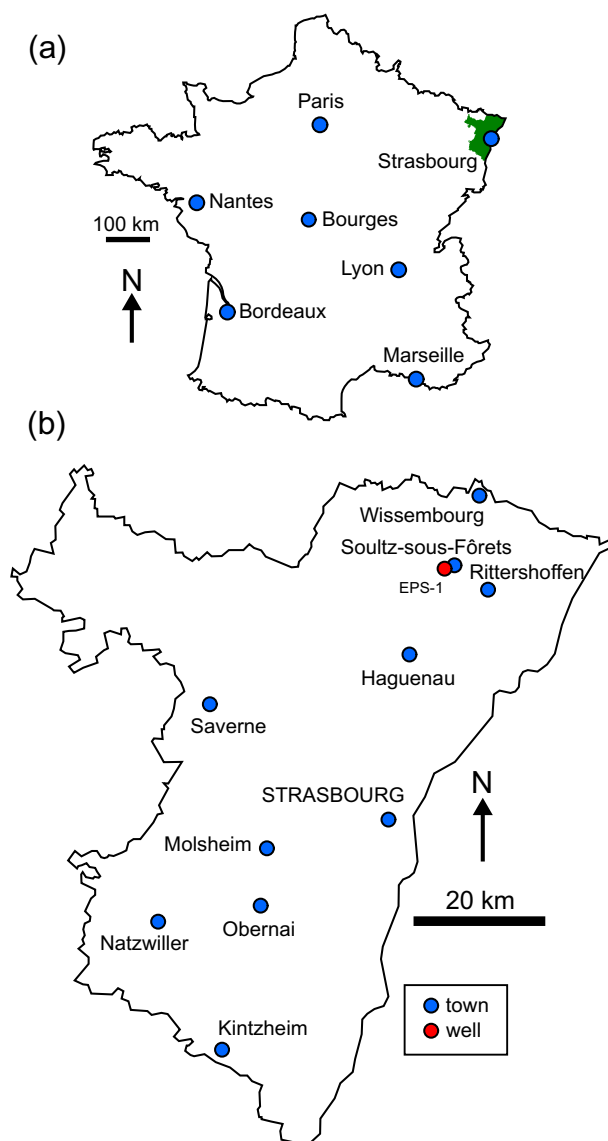


**Fig. 1** **a** Map of France showing location of Alsace (in green). **b** Map of Alsace showing the location of Sultz-sous-Forêts and exploration borehole EPS-1. Modified from Heap et al. (2017)

Whether the Buntsandstein sandstone of the Upper Rhine Graben is characterised by a permeability anisotropy, and the magnitude of this anisotropy, is currently unknown. Knowledge of the presence and magnitude of permeability anisotropy is a key parameter to help move towards more realistic models of hydrothermal convection in the Upper Rhine Graben, allowing for the optimisation of geothermal energy exploitation.

## Materials

### Core descriptions

The materials used in this study were extracted from exploration well EPS-1 at the Soultz-sous-Forêts geothermal site in north-eastern France (Fig. 1). Seven sandstone cores from the Buntsandstein, with a diameter of 78 mm, were used: three from the Karlstal unit (box numbers 176, 189, and 190) and four from the Rehberg unit (box numbers 254, 257, 285, and 356) (Fig. 2). The Karlstal and Rehberg units are thought to be aeolian and fluvial sandstones, respectively (Aichholzer et al. 2016). These seven cores, taken from depths between 1086 and 1247 m (Fig. 2), were selected due to their visible anisotropy (i.e. bedding and laminations; Fig. 3). In this study, we will refer to each core by their box number.

All cores contain laminations, darker in colour than the host-rock, that are perpendicular or sub-perpendicular to the core axis (Fig. 3). Laminations sets (containing from several to tens of individual laminations that are less than a millimetre thick) vary from 5 to 10 mm in thickness with a typical spacing of 5 to 20 mm. The laminations and

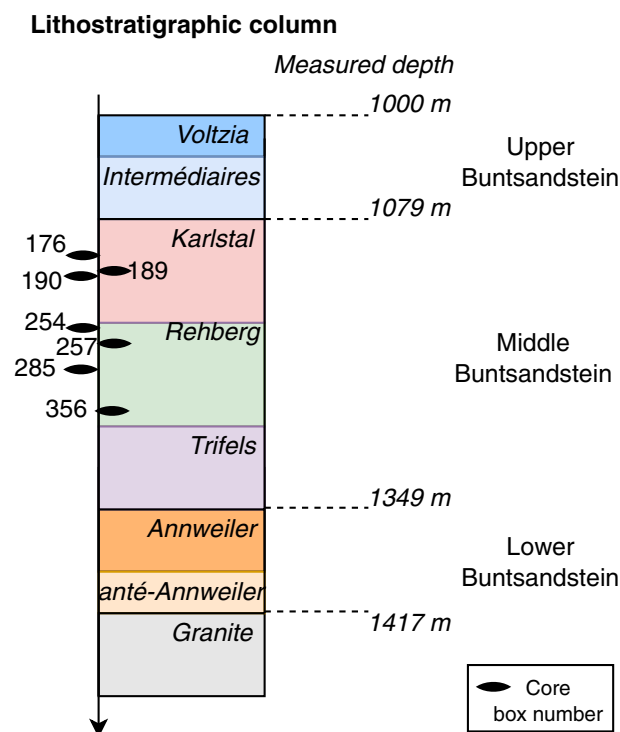


**Fig. 2** Lithostratigraphic column for Buntsandstein in exploration borehole EPS-1 (Soultz-sous-Forêts) showing the location of the sampling depths (black ellipses). The box number is given next to each sampling depth (176, 189, 190, 254, 257, 285, and 356). Depths and unit names provided by Aichholzer et al. (2016)

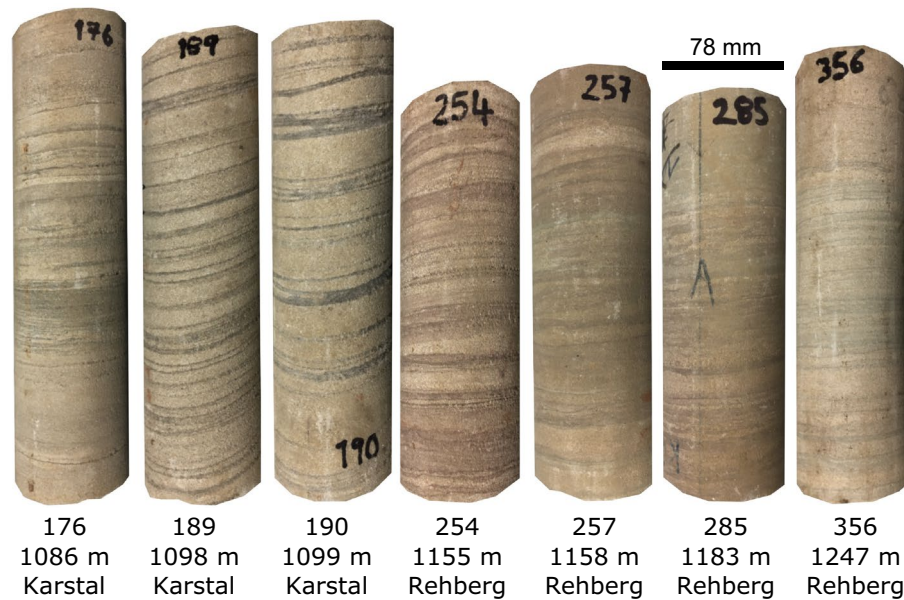


**Fig. 3** Photographs of the visibility anisotropic 78-mm-diameter cores sampled from exploration borehole EPS-1 (Soulz-sous-Forêts). The box number, depth, and lithostratigraphic unit are provided next to each core

lamination sets can be planar (e.g., cores 189 and 356) or wavy (e.g., cores 176, 254, 257, and 285). The lamination sets are more-or-less regularly spaced for all the cores, except for cores 190 and 356. The lamination sets in cores 190 and 356 are grouped, where each group consists of about five lamination sets with a spacing of 5 mm or less that are separated by 20-mm-thick layers of host-rock. The lamination sets are less pronounced, and are only 1 to 2 mm in thickness, in core 257. The laminations and lamination sets in some cores, 176 and 254 in particular, are slightly eroded, suggesting that they are weaker than the host-rock. We note that the grain size appears to be smaller in the laminations than the host-rock and that, for all cores, there are no visible fractures.

#### Sample descriptions

Forty-two cylindrical rock samples, 20 mm in diameter and 40 mm in length, were prepared from the seven cores (Fig. 4). Six samples, three perpendicular to bedding (samples 1, 2, and 3) and three parallel to bedding (samples 4, 5, and 6), were prepared from each core. Samples from cores 190 and 356 were cored from the layers containing the groups of laminations. All the samples were first washed and dried in a vacuum oven at 40 °C. All of the prepared samples contain either laminations perpendicular/sub-perpendicular or parallel/sub-parallel to the sample axis (Fig. 4). The number of laminations for the samples cored perpendicular and parallel to bedding varied from 4 to 14 and 2–8, respectively, and the thickness of individual laminations varied from 0.1 mm to up to almost one millimetre (Fig. 4).

#### Microstructural descriptions

Thin sections were prepared for each core and their microstructure was examined using an optical microscope (Fig. 5). All samples are mainly composed of quartz, feldspar, and clay. The laminations are easy to distinguish on the thin section images due to the

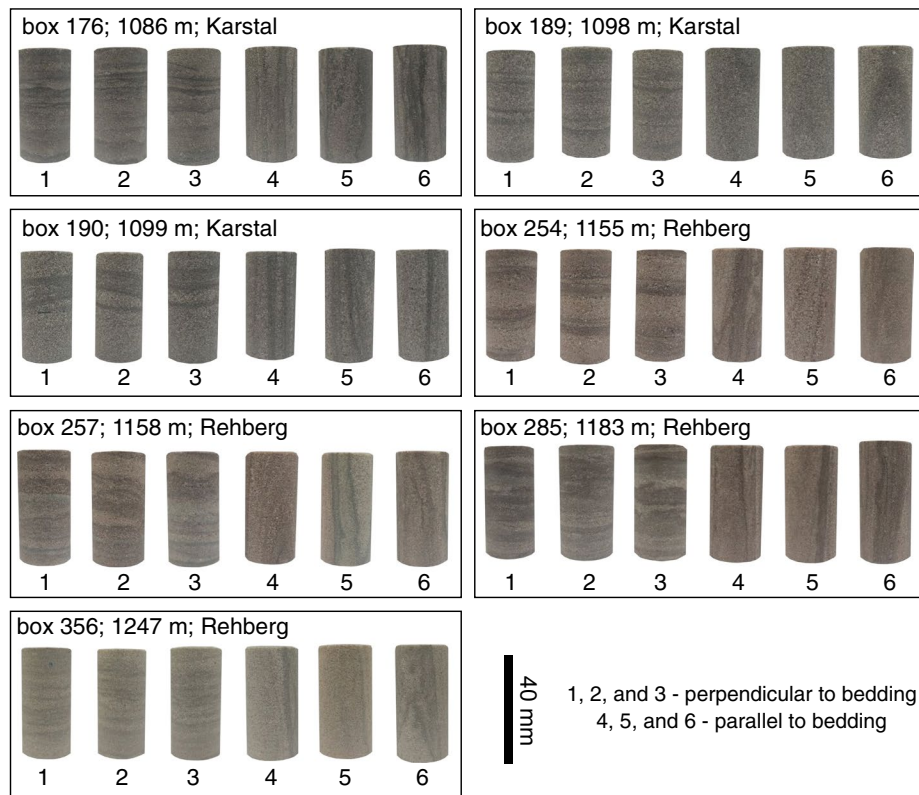


**Fig. 4** Photographs of the 20-mm-diameter cylindrical core samples prepared from the seven cores shown in Fig. 3. Six samples were prepared from each core: three perpendicular to bedding (samples 1, 2, and 3) and three parallel to bedding (samples 4, 5, and 6). The box number, depth, and lithostratigraphic unit are provided next to each set of samples

differences in the grain size between the laminations and the host-rock. The grain size within the laminations is typically much smaller than the host-rock. The grain size difference between the laminations and the host-rock is particularly evident in sample 254 (Fig. 5d). The images of sample 254 also show how the thickness of the laminations can vary within a sample (compare Fig. 5d, e). As noted in our core and sample descriptions, we also see that the laminations can be planar or wavy in thin section. A quantitative description of the microstructure is provided later in the manuscript.

## Methods

### Laboratory methods

Although permeability was the main focus of this study, we also measured the porosity and P-wave velocity of each of our samples. The connected porosity of each cylindrical sample was determined using the bulk sample volume and the skeletal volume measured using a helium pycnometer (Micromeritics AccuPyc II 1340). We also estimated the total porosity of the samples using the dry bulk density and the density of quartz ( $2650 \text{ kg/m}^3$ ), the most abundant mineral in the studied sandstones (Fig. 5).

P-wave velocity was measured on dry samples using two piezoelectric sensors, a function generator (using a frequency of 700 kHz), and an oscilloscope (see schematic

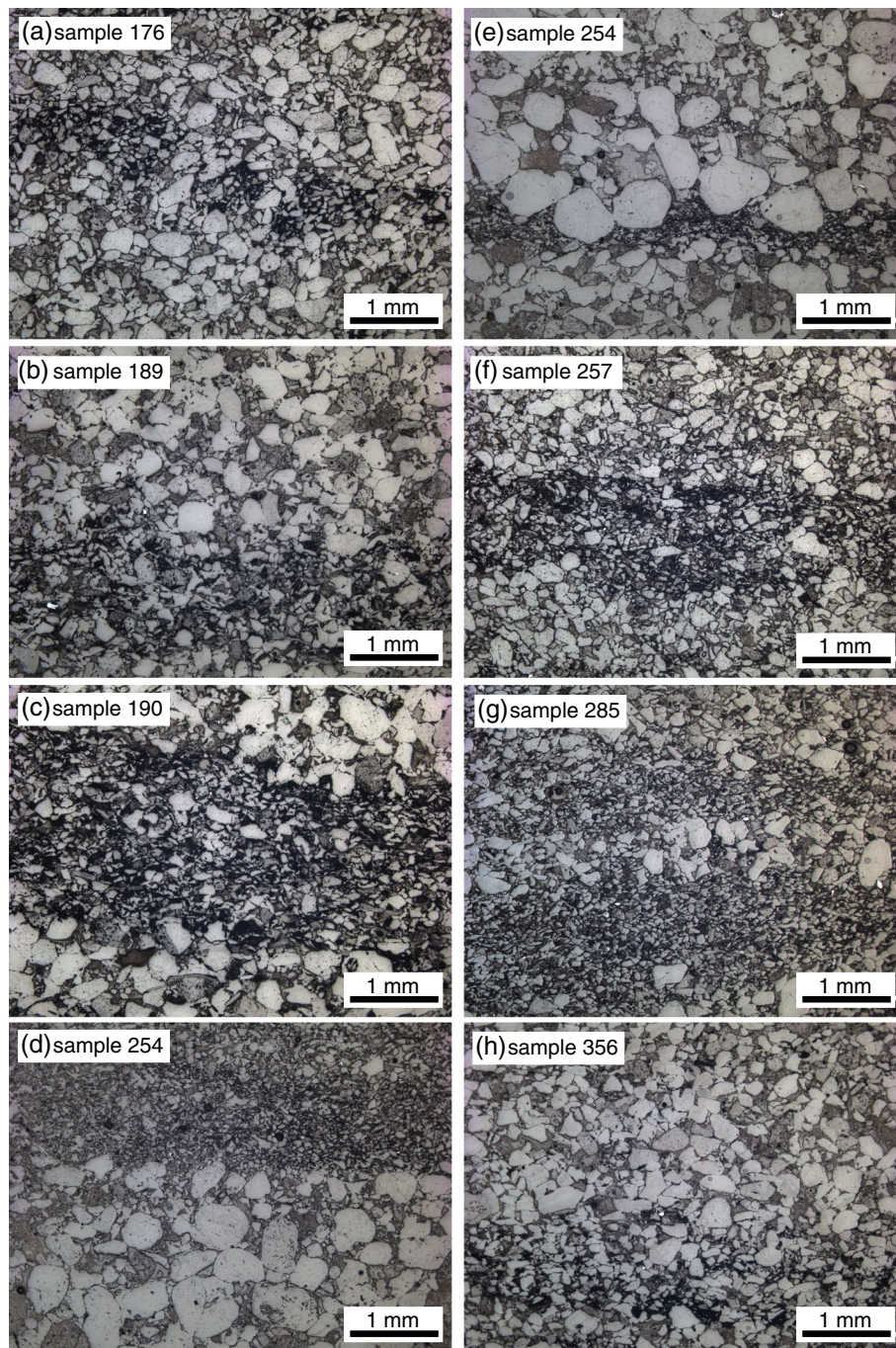


**Fig. 5** Microstructural images of the seven cores investigated in this study (shown in Fig. 3) taken using an optical microscope under reflected light. **a** Sample 176. **b** Sample 189. **c** Sample 190. **d** Sample 254. **e** Sample 254. **f** Sample 257. **g** Sample 285. **h** Sample 356

diagram in Heap et al. 2014). P-wave velocity was measured along the axis of each of the samples under ambient laboratory pressure and temperature. To ensure a good connection between the sample and the endcaps, we applied an axial force of 300 N.

The permeability of each sample was measured using a benchtop gas permeameter (see schematic diagram in Farquharson et al. 2016; Heap and Kennedy 2016). This permeameter is capable of measuring the permeability of cylindrical samples that are 10–25 mm in diameter and 10–60 mm in length (Heap 2019). Unlithified granular materials can also be measured in this setup, using a rubber jacket of known internal volume and two metal endcaps (as in Heap et al. 2020). Permeability was measured at ambient laboratory temperature under a confining pressure of 1 MPa (to ensure that the gas passes through the sample and not around the sides). We waited one hour before starting the measurements to ensure microstructural equilibrium. Depending on the permeability of the sample, measurements were made using either the steady-state method (for high-permeability samples) or the pulse-decay method (for low-permeability samples). For the steady-state method, we measured volumetric flow rates (measured using a gas flowmeter) for six different pore pressure differentials (measured using a pressure transducer). For the pulse-decay method, we monitored the pressure decay of an upstream reservoir (measured using a pressure transducer) as a function of time (Brace et al. 1968). These data were then used to calculate Darcy's law and to check whether the Klinkenberg or Forchheimer corrections were needed. All the equations used for the calculation of permeability can be found in Heap et al. (2017).

### Microstructural analysis

We performed grain size and shape analysis on optical microscope images of each of the studied sandstones using open-source image analysis software ImageJ. Grain size and shape analysis was performed on both the laminations and host-rock for each sample. First, we manually drew around all the grains within selected images using open-source vector graphics program Inkscape. The grains were then coloured black and the resultant image was imported into and analysed using ImageJ. The number of grains analysed per layer ranged from 259 to 1063. Using ImageJ, we determined the equivalent grain diameter, grain area, grain circularity, and grain aspect ratio. The equivalent grain diameter,  $d$ , of each grain was calculated using  $d = 3/2(d_F)$ , where  $d_F$  is the average Feret diameter. The aspect ratio of each grain was calculated as the major divided by the minor grain axis. The circularity of each grain,  $C$ , was calculated using  $C = 4\pi A/P^2$ , where  $A$  and  $P$  are the grain area and perimeter, respectively. A circularity,  $C$ , of one corresponds to a perfect circle.

## Results

### Porosity

Connected porosity measurements gave values ranging from 5.2 to 16.3% (Fig. 6; Table 1). Total porosity as a function of connected porosity is shown in Fig. 6. The data of Fig. 6 show that the difference between the connected porosity and the total porosity is almost equal to zero, and therefore that there is negligible isolated porosity in the studied sandstones. Small differences between the connected porosity and the total porosity are likely the result of the assumption of 100% quartz in the determination of total porosity (we note that the samples also contain some feldspars and clays; Fig. 5).



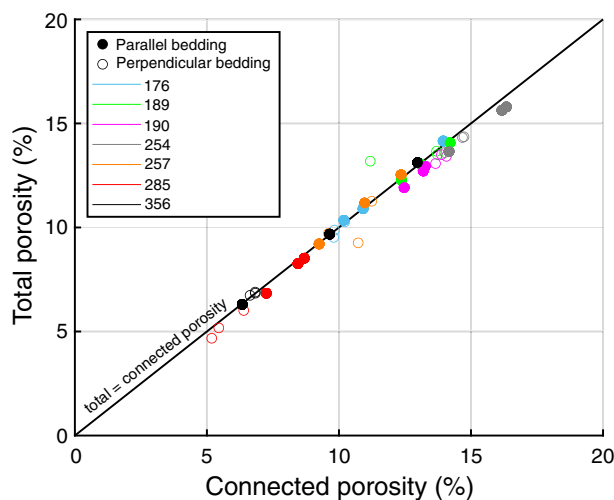


**Fig. 6** Total porosity as a function of connected porosity for the 42 samples of Buntsandstein sandstone prepared for this study. Samples were prepared either parallel (filled circles) or perpendicular (unfilled circles) to bedding. The number refers to the box number

### Grain size and shape analyses

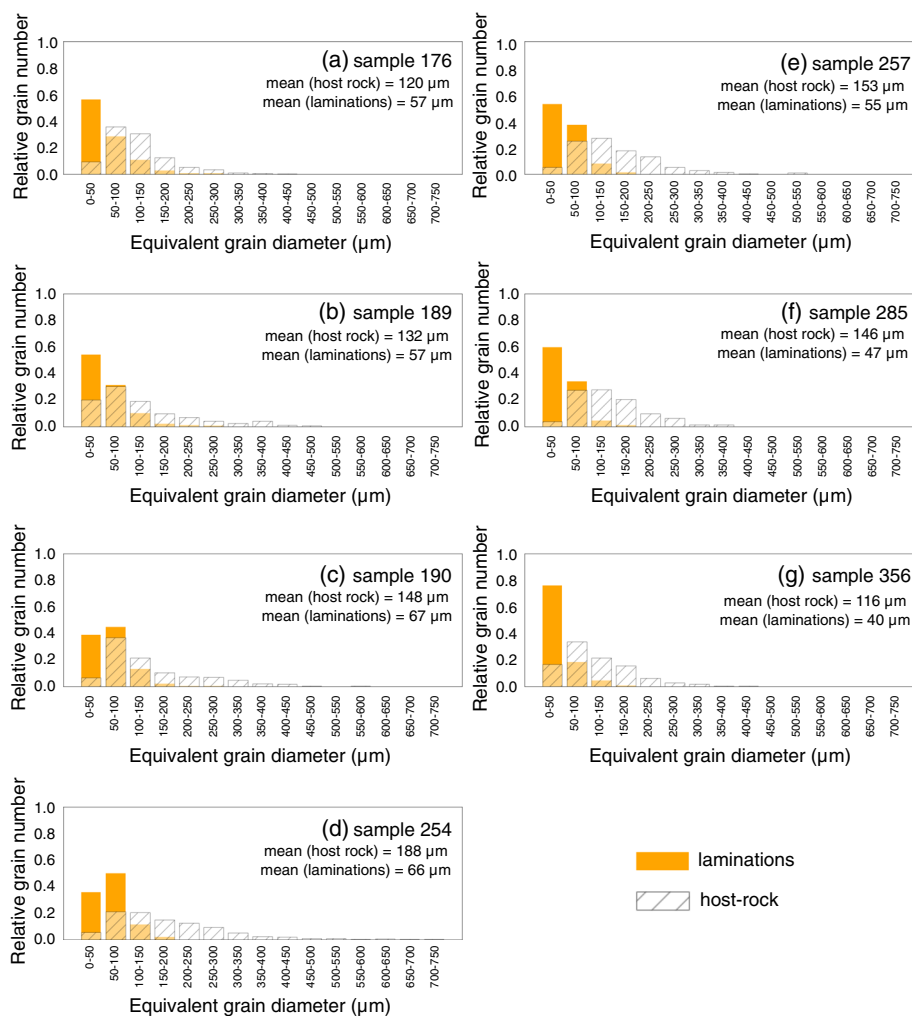
Figure 7 shows a histogram of the distribution of equivalent grain diameter of each of the studied sandstones (the mean equivalent grain diameter for each layer is also provided on the graphs). For each sandstone, we provide distributions for both the laminations (orange bars) and the host-rock (shaded bars). For all of the samples, the grain size distribution for the laminations is very different to that of the host-rock. For the laminations, the grain diameter ranges from 0 to 300  $\mu\text{m}$ , but the majority of grains are between 0 and 150  $\mu\text{m}$ . In general, the most abundant grain size for the laminations is 0–50  $\mu\text{m}$  (this is true for all samples except samples 257 and 285). For the host-rock, the grain diameter ranges from 0 to 750  $\mu\text{m}$  and, therefore, the distribution of grain size within the host-rock is much larger than that for the laminations. Sample 254 is the only sample to contain grains up to a diameter of 750  $\mu\text{m}$  (grain diameter typically ranges from 0 to 500  $\mu\text{m}$  for the other samples) and is therefore the most heterogeneous sample. In general, the most abundant grain size for the host-rock is 50–100  $\mu\text{m}$  (this is true for all samples except samples 190 and 254). For all cores, the average grain size is much smaller in the laminations than in the host-rock.

Figure 8 shows a histogram of the distribution of grain area of each of the studied sandstones. We again provide distributions for both the laminations (orange bars) and the host-rock (shaded bars). The data of Fig. 12 allow us to see which grain diameter range corresponds to the largest area. For example, for the laminations in sample 176, Fig. 7 shows us that the largest number of grains have a diameter of 0–50  $\mu\text{m}$ . However, in terms of area, the most abundant grain diameter range is 100–150  $\mu\text{m}$ . Similarly, the laminations in sample 356 contain a lot of very small grains (80% of the grains are 0–50  $\mu\text{m}$ ), but the most representative grain diameter range in terms of area is 50–100  $\mu\text{m}$ . For all the samples (and for both layers), the most abundant grain

**Table 1** Depth, lithostratigraphic unit, sample orientation, connected porosity, total porosity, P-wave velocity, and permeability for each of the 42 Buntsandstein samples prepared for this study

Sample number	Depth (m)	Unit	Orientation	Connected porosity (%)	Total porosity (%)	P-wave velocity (km/s)	Permeability (m <sup>2</sup> )
176 1	1086	Karlstal	Perpendicular	9.8	9.5	3.25	$2.02 \times 10^{-17}$
176 2	1086	Karlstal	Perpendicular	9.8	9.9	3.25	$2.99 \times 10^{-17}$
176 3	1086	Karlstal	Perpendicular	10.2	10.3	3.16	$4.50 \times 10^{-17}$
176 4	1086	Karlstal	Parallel	13.9	14.2	3.69	$4.43 \times 10^{-16}$
176 5	1086	Karlstal	Parallel	10.9	10.9	3.72	$1.22 \times 10^{-16}$
176 6	1086	Karlstal	Parallel	10.2	10.3	3.76	$5.64 \times 10^{-17}$
189 1	1098	Karlstal	Perpendicular	13.7	13.5	3.71	$2.35 \times 10^{-17}$
189 2	1098	Karlstal	Perpendicular	13.7	13.7	3.52	$3.61 \times 10^{-17}$
189 3	1098	Karlstal	Perpendicular	11.2	13.2	3.60	$6.31 \times 10^{-17}$
189 4	1098	Karlstal	Parallel	13.1	13.0	3.79	$7.66 \times 10^{-14}$
189 5	1098	Karlstal	Parallel	12.4	12.3	3.81	$7.42 \times 10^{-14}$
189 6	1098	Karlstal	Parallel	14.2	14.1	3.88	$5.36 \times 10^{-16}$
190 1	1099	Karlstal	Perpendicular	13.9	13.5	3.43	$3.58 \times 10^{-17}$
190 2	1099	Karlstal	Perpendicular	14.1	13.4	3.31	$3.22 \times 10^{-17}$
190 3	1099	Karlstal	Perpendicular	13.6	13.1	3.31	$5.39 \times 10^{-17}$
190 4	1099	Karlstal	Parallel	12.5	11.9	3.95	$4.43 \times 10^{-15}$
190 5	1099	Karlstal	Parallel	13.2	12.7	3.94	$3.86 \times 10^{-16}$
190 6	1099	Karlstal	Parallel	13.3	12.9	4.16	$7.31 \times 10^{-14}$
254 1	1155	Rehberg	Perpendicular	14.7	14.3	3.43	$1.56 \times 10^{-16}$
254 2	1155	Rehberg	Perpendicular	14.7	14.3	3.35	$1.07 \times 10^{-16}$
254 3	1155	Rehberg	Perpendicular	14.0	13.6	3.49	$1.83 \times 10^{-16}$
254 4	1155	Rehberg	Parallel	14.2	13.6	3.99	$1.32 \times 10^{-15}$
254 5	1155	Rehberg	Parallel	16.3	15.8	3.81	$1.43 \times 10^{-14}$
254 6	1155	Rehberg	Parallel	16.2	15.6	4.04	$7.03 \times 10^{-14}$
257 1	1158	Rehberg	Perpendicular	9.6	9.7	3.21	$3.80 \times 10^{-17}$
257 2	1158	Rehberg	Perpendicular	11.2	11.3	3.24	$7.69 \times 10^{-17}$
257 3	1158	Rehberg	Perpendicular	10.7	9.2	3.23	$1.90 \times 10^{-17}$
257 4	1158	Rehberg	Parallel	12.3	12.5	3.55	$2.02 \times 10^{-15}$
257 5	1158	Rehberg	Parallel	10.9	11.2	4.07	$5.67 \times 10^{-16}$
257 6	1158	Rehberg	Parallel	9.2	9.2	3.71	$1.79 \times 10^{-16}$
285 1	1183	Rehberg	Perpendicular	5.2	4.7	3.72	$2.45 \times 10^{-17}$
285 2	1183	Rehberg	Perpendicular	5.4	5.2	3.85	$1.46 \times 10^{-17}$
285 3	1183	Rehberg	Perpendicular	6.4	6.0	3.80	$2.00 \times 10^{-17}$
285 4	1183	Rehberg	Parallel	8.4	8.3	4.20	$2.18 \times 10^{-16}$
285 5	1183	Rehberg	Parallel	8.7	8.5	4.20	$3.10 \times 10^{-17}$
285 6	1183	Rehberg	Parallel	7.2	6.8	4.34	$8.20 \times 10^{-17}$
356 1	1247	Rehberg	Perpendicular	6.8	6.9	3.32	$2.48 \times 10^{-18}$
356 2	1247	Rehberg	Perpendicular	6.6	6.7	3.28	$5.88 \times 10^{-18}$
356 3	1247	Rehberg	Perpendicular	6.8	6.8	3.27	$4.19 \times 10^{-18}$
356 4	1247	Rehberg	Parallel	6.3	6.3	4.19	$3.22 \times 10^{-17}$
356 5	1247	Rehberg	Parallel	12.9	13.1	3.71	$2.95 \times 10^{-17}$
356 6	1247	Rehberg	Parallel	9.6	9.7	3.88	$7.81 \times 10^{-18}$

diameter interval in terms of area is different to that in terms of number. The only exception is for samples 257 and 285, for which the two most abundant ranges (area and number) are the same for the laminations.



**Fig. 7** Histograms showing relative grain number as a function of equivalent grain diameter for each of the seven cores investigated in this study (shown in Fig. 3). **a** Sample 176. **b** Sample 189. **c** Sample 190. **d** Sample 254. **e** Sample 257. **f** Sample 285. **g** Sample 356. The orange bars show the grain size distribution in the laminations and the shaded bars show the grain size distribution in the host-rock

We find that grain circularity and aspect ratio do not differ significantly between samples and between the different layers (laminations and host-rock). Grain circularity ranges from 0.69 to 0.73 and from 0.69 to 0.77 for the host-rock and laminations, respectively. Grain aspect ratio ranges from 1.72 to 1.85 and from 1.81 to 1.98 for the host-rock and laminations, respectively.

#### Permeability and P-wave velocity

Permeability and P-wave velocity are plotted as a function of connected porosity in Fig. 9a, b, respectively (data available in Table 1). In general, permeability increases as a function of increasing porosity (Fig. 9a). Permeability increases from  $2.48 \times 10^{-18}$  to  $7.66 \times 10^{-14} \text{ m}^2$  as porosity increases from 5.2 to 16.3%. Figure 9a also shows that for samples with laminations parallel to the sample axis and therefore flow direction (filled circles), permeability is consistently higher than for samples with perpendicular

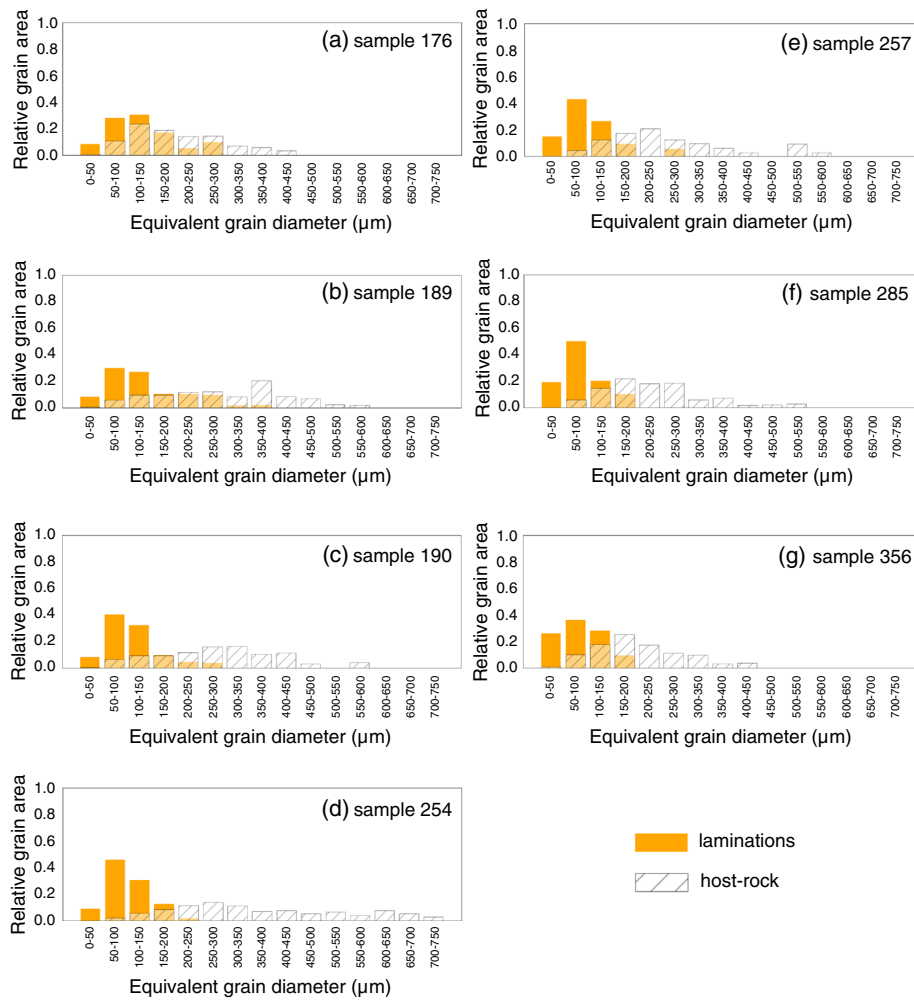


**Fig. 8** Histograms showing relative grain area as a function of equivalent grain diameter for each of the seven cores investigated in this study (shown in Fig. 3). **a** Sample 176. **b** Sample 189. **c** Sample 190. **d** Sample 254. **e** Sample 257. **f** Sample 285. **g** Sample 356. The orange bars show the grain area distribution in the laminations and the shaded bars show the grain area distribution in the host-rock

laminations (unfilled circles). Samples 254\_6, 190\_6, 189\_4, and 189\_5 (all containing laminations parallel to the sample axis) have the highest permeability values ( $10^{-14} \text{ m}^2$ ). We further note that the permeability of samples with perpendicular laminations is within a narrow range (i.e. the values too close to one another), whereas the permeability of the samples with parallel laminations can vary by a couple of orders of magnitude. Indeed, a few datapoints for samples with parallel laminations are close in permeability to samples with perpendicular laminations from the same core.

In general, P-wave velocity decreases as a function of increasing porosity (Fig. 9b), but the trend is much less pronounced than for the permeability data. P-wave velocity ranges from 3.16 to 4.34 km/s for a porosity ranging from 5.2 to 16.3%, and can vary by up to 1 km/s at low porosity (< 10%). P-wave velocity values for samples with parallel laminations (filled circles) are consistently higher (from 0.2 to 0.8 km/s) than those measured on samples with perpendicular laminations (unfilled circles).

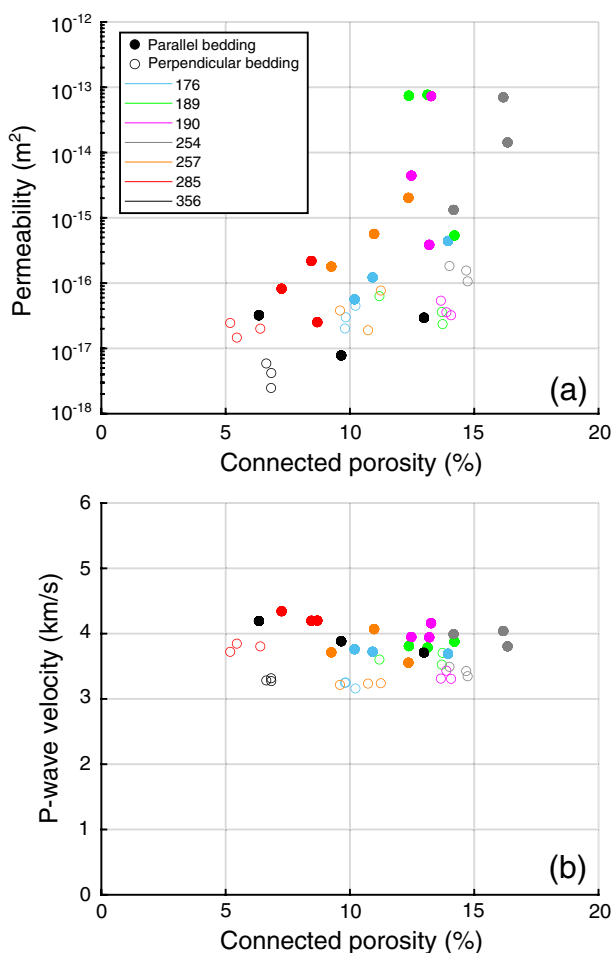


**Fig. 9** **a** Permeability and **b** P-wave velocity as a function of connected porosity for the 42 samples of Buntsandstein sandstone prepared for this study. Samples were prepared either parallel (filled circles) or perpendicular (unfilled circles) to bedding. The number refers to the box number

In order to better illustrate the permeability anisotropy, we plot a permeability ratio ( $k_{\text{perp}}/k_{\text{para}}$ ) as a function of the connected porosity in Fig. 10a. To do so, samples were grouped into pairs, one with perpendicular laminations and one with parallel laminations. The pairs of samples were selected based on their porosities. The permeability ratio is defined as the ratio of the permeability of the sample containing perpendicular laminations to the permeability of the sample containing parallel laminations. The permeability ratio values for our samples ranges from 0.0004 to 0.30 (Fig. 10a). We first note that the permeability ratio for all our samples is below one (i.e. the permeability parallel to the laminations is always higher than the permeability perpendicular to the laminations). Second, we highlight that the permeability ratio decreases as a function of increasing porosity. In other words, the high-porosity samples are more anisotropic, in terms of their permeability, than the low-porosity samples. Finally, we note that the anisotropy value can vary between samples prepared from the same core. For example, the permeability ratio of samples 190 (pink circles) and 254 (grey circles) varies between 0.0004 and 0.083 and between 0.002 and 0.14,

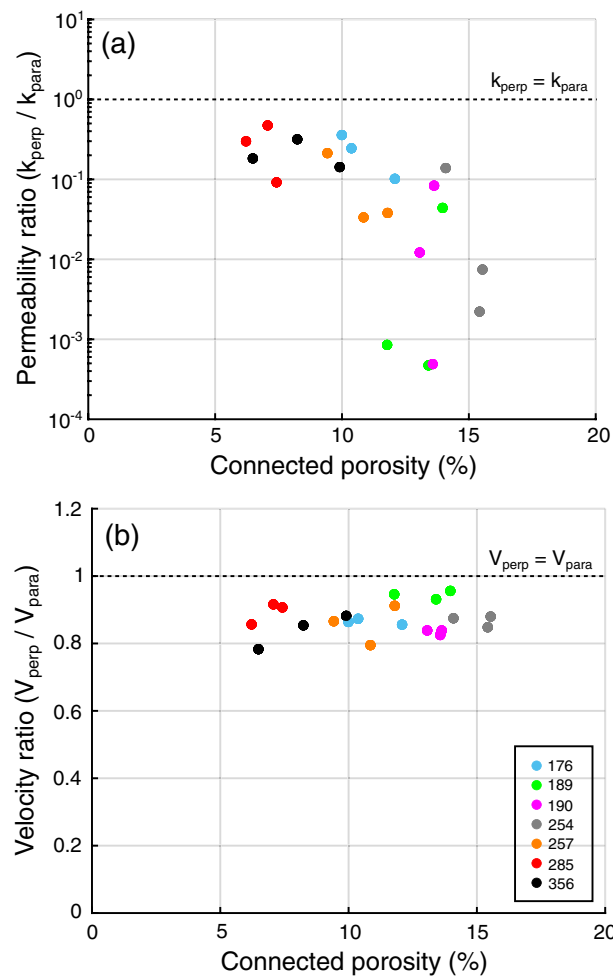


**Fig. 10** **a** Permeability ratio and **b** P-wave velocity ratio as a function of connected porosity for the Buntsandstein sandstone samples prepared for this study. The number refers to the box number

respectively. The permeability ratio can vary a lot for the high-porosity samples, but does not vary considerably for the low-porosity samples (Fig. 10a).

In order to better illustrate the P-wave velocity anisotropy, we plot a P-wave ratio (the ratio of the P-wave velocity of the sample containing perpendicular laminations to the P-wave velocity of the sample containing parallel laminations) as a function of the connected porosity in Fig. 10b. The P-wave velocity ratio values for our samples range from 0.85 and 0.88. All our P-wave velocity ratios are below one, and so the P-wave velocity parallel to the laminations is always higher than the P-wave velocity perpendicular to the laminations. However, there is no discernible trend between P-wave velocity ratio and porosity. We also note that, unlike the permeability data shown in Fig. 10a, variations in P-wave velocity ratio between samples prepared from the same core are small (Fig. 10b).

## Discussion

### Permeability and P-wave velocity as a function of porosity

Permeability is plotted as a function of porosity in Fig. 11a, together with previously published data for Buntsandstein sandstones from EPS-1 (Griffiths et al. 2016; Heap

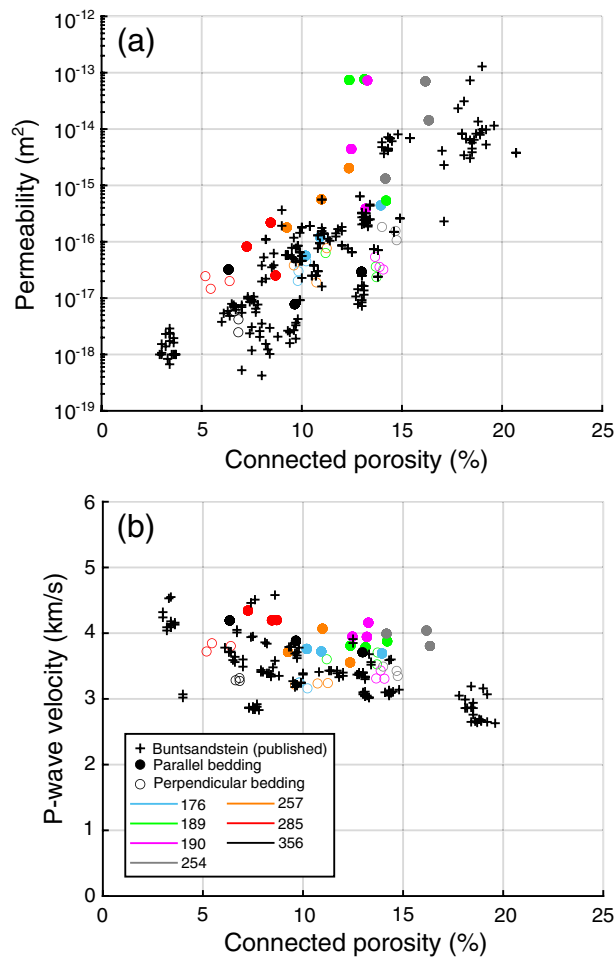


**Fig. 11** **a** Permeability and **b** P-wave velocity as a function of connected porosity for the 42 samples of Buntsandstein sandstone prepared for this study, together with previously published data for Buntsandstein sandstone samples taken from EPS-1 (Soultz-sous-Forêts) (data from Griffiths et al. 2016; Heap et al. 2017, 2019a; Kushnir et al. 2018b). Samples were prepared either parallel (filled circles) or perpendicular (unfilled circles) to bedding. The number refers to the box number

et al. 2017; Kushnir et al. 2018b). The permeability values obtained in this study are in broad agreement with those previously published for the Buntsandstein (Fig. 11a). We find, in agreement with data for the Buntsandstein (Griffiths et al. 2016; Heap et al. 2017; Kushnir et al. 2018b) and other sandstones (Bourbié and Zinszner 1985; Nelson 1994; Ehrenberg and Nadeau 2005; Wadsworth et al. 2016), that permeability increases as a function of increasing porosity (Figs. 9, 11a).

P-wave velocity is plotted as a function of porosity in Fig. 11b, together with previously published data for Buntsandstein sandstones from EPS-1 (Heap et al. 2017, 2019a). Although we do not observe a clear trend in P-wave velocity as a function of porosity (Fig. 9b), our data are in general agreement with those previously published (Fig. 11b). We conclude that the absence of a trend in our P-wave velocity data is likely that result of the narrow range in porosity (between 5.2 and 16.3%) and that, if more samples were measured that contain higher or lower porosities, we would likely see a trend of decreasing P-wave velocity as a function of increasing porosity, as expected for sandstones (Han

et al. 1986; Eberhardt-Phillips et al. 1989; Chang et al. 2006; Vasseur et al. 2016; Hill et al. 2022).

**Permeability anisotropy**

Permeability ratio is plotted as a function of porosity in Fig. 12a, together with previously published data for Buntsandstein sandstones from EPS-1 (black crosses; Griffiths et al. 2016; Heap et al. 2017) and other sandstones (grey squares; Benson et al. 2005; Clavaud et al. 2008; Baud et al. 2012; Meng et al. 2021). While our permeability ratio varies from 0.0004 to 0.30, the published permeability ratio for sandstones (Buntsandstein sandstone and other sandstones) ranges from 0.04 to 3.49. Therefore, not only are these published data much less anisotropic than the sandstones studied herein, the permeability of some samples is higher when measured perpendicular to bedding (those samples with permeability ratios above one). The higher permeability anisotropy in our samples, compared

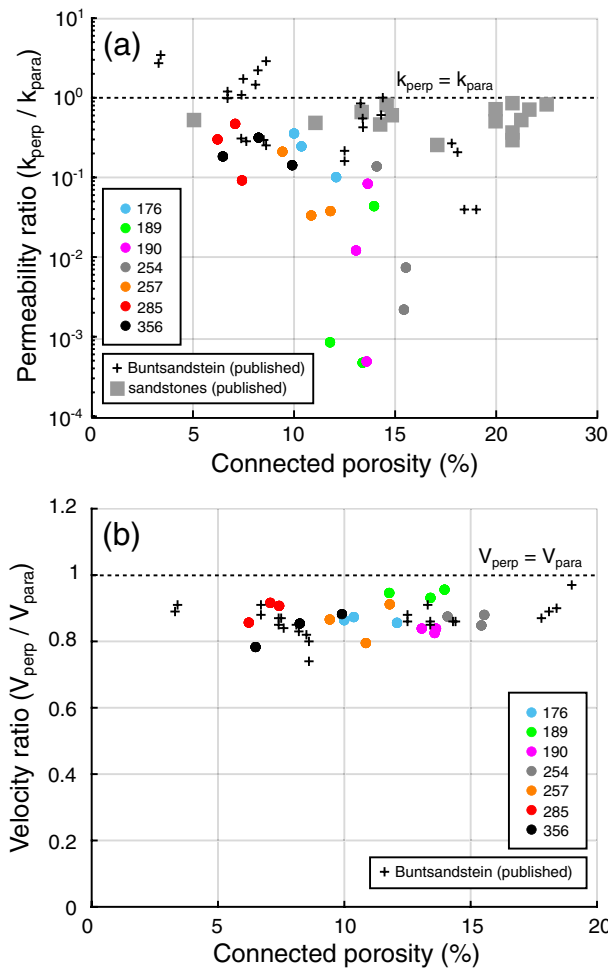


**Fig. 12** **a** Permeability ratio and **b** P-wave velocity ratio as a function of connected porosity for the Buntsandstein sandstone samples prepared for this study, together with previously published data for Buntsandstein sandstone samples taken from EPS-1 (Soulz-sous-Forêts) (black crosses; data from Griffiths et al. 2016; Heap et al. 2017) and other sandstones (grey squares; data from Benson et al. 2005; Clavaud et al. 2008; Baud et al. 2012; Meng et al. 2021). The number refers to the box number



to previously published data, can be explained by the fact that we purposely selected the most visibly anisotropic samples from EPS-1 for our study (Fig. 4). Our new data, therefore, extend the expected range of permeability anisotropy in sandstones resulting from bedding/laminations. We suggest that permeability ratios above one from Griffiths et al. (2016) and Heap et al. (2017) likely reflect sample variability (differences in sample porosity), rather than a permeability that is higher perpendicular to bedding. Although the published data for Buntsandstein sandstone show that the more porous samples are typically more anisotropic in terms of their permeability, as observed in our new dataset, we note that the published data for sandstone with a porosity > 20% are characterised by a low-permeability anisotropy, despite their high porosities (Fig. 12a). We consider this as a difference between permeability anisotropy resulting from low-permeability laminations, which can significantly reduce the permeability of high-porosity sandstones, and permeability anisotropy resulting from a preferred pore shape orientation, which only results in a mild permeability anisotropy. We will now discuss why our samples are anisotropic, why there is a large range in the permeability of the samples containing parallel laminations, and why the more porous sandstones are more anisotropic.

Our microstructural observations and analyses highlighted that, for all of our samples, the laminations are characterised by a smaller grain size than the host-rock (Figs. 5, 6, 7, 8). Previous studies have shown that, typically, the permeability of granular materials and granular rocks is reduced as a function of decreasing average grain size (Masch and Denny 1966; Shepherd 1989; Wadsworth et al. 2016). To better understand whether the smaller grain size of the laminations could explain the observed permeability anisotropy, we estimated the permeability of the laminations and host-rock for each sample using a model for the permeability of monodisperse granular materials (Wadsworth et al. 2016). The permeability,  $k_D$ , of the laminations and host-rock for each sample was modelled using (Martys et al. 1994; Wadsworth et al. 2016):

$$k_D = \frac{2\phi}{s^2} (\phi - \phi_c)^b, \quad (1)$$

where  $\phi_c$  is the porosity at the percolation threshold (assumed here to be 0.03; see Wadsworth et al. 2016),  $b$  is a constant related to the particle geometry (assumed here to be 4.2; see Wadsworth et al. 2016), and  $s$  is the specific surface. We determine  $s$  by calculating an effective pore radius,  $a$ , for a given non-overlapping monodisperse grain radius using (Wadsworth et al. 2016):

$$s(a) = \frac{3(1 - \phi)\ln(1 - \phi)}{a}. \quad (2)$$

To calculate  $a$ , and therefore  $s$ , for the laminations and host-rock of each sample, we used the mean grain size from our microstructural analysis (Fig. 7). The results of the modelling, which assumes the same porosity,  $\phi$ , for the laminations and host-rock (that of the sample), are provided in Table 2. The permeability modelling shows that the permeability of the laminations is always lower than that of the host-rock. We highlight that the differences in modelled permeability between the laminations and host-rock (Table 2) is likely an underestimation, as it is also likely that the porosity of the laminations is lower than that of the host-rock. Since the laminations have a

**Table 2** Modelled permeabilities for the laminations and host-rock from each of the seven Buntsandstein cores investigated in this study using a model for the permeability of monodisperse granular media (Wadsworth et al. 2016). See text for details

Core box number	Modelled laminations permeability (m <sup>2</sup> )	Modelled host-rock permeability (m <sup>2</sup> )
176	$5.3 \times 10^{-14}$	$2.4 \times 10^{-13}$
189	$9.2 \times 10^{-14}$	$5.0 \times 10^{-13}$
190	$1.3 \times 10^{-13}$	$6.5 \times 10^{-13}$
254	$1.9 \times 10^{-13}$	$1.5 \times 10^{-12}$
257	$5.0 \times 10^{-14}$	$3.8 \times 10^{-13}$
285	$1.1 \times 10^{-14}$	$1.0 \times 10^{-13}$
356	$1.2 \times 10^{-14}$	$1.0 \times 10^{-13}$

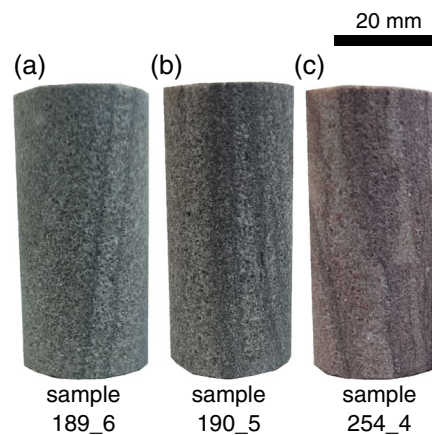


**Fig. 13** Photographs of three of the measured 20-mm-diameter cylindrical core samples (samples 189\_6, 190\_5, and 254\_4) that show laminations that are sub-parallel or oblique to the core axis

permeability lower than the host-rock, when they are orientated perpendicular to the direction of fluid flow (i.e. in series), the permeability of the sample will be close to that of the laminations. However, when the low-permeability laminations are oriented parallel to the direction of fluid flow (i.e. in parallel), the permeability of the sample will be close to that of the host-rock. This explains why our samples are characterised by a permeability anisotropy.

As noted previously, the permeability of samples with parallel laminations from the same core can vary by a couple of orders of magnitude (Fig. 9a). In particular, samples 189, 190, and 254 contain one sample with parallel laminations that has a permeability much lower than the other samples with parallel laminations. The permeability of these samples is close to the permeability of the samples with perpendicular laminations. A closer inspection of these outlying samples shows that the laminations are not strictly parallel to the axis of the sample (Fig. 13). A sub-parallel, or oblique, low-permeability lamination can act as a barrier to fluid flow if it cross-cuts the sample. This explains why some of the samples with parallel laminations have permeability values close to the samples with perpendicular laminations, and why we see a large variation in the permeability of samples with parallel laminations.

Our data show that the more porous samples are more anisotropic (Figs. 9, 10a). This can be explained by the fact that the permeability of a sample with a higher host-rock permeability will be more impacted by the presence of a low-permeability layer. In other words, the difference between the permeability of the sample with parallel laminations (which will be close to the permeability of the highly permeable host-rock) and the permeability of the sample with perpendicular laminations (which will be close to the permeability of the low-permeability lamination) will be large. By contrast, the impact of a low-permeability lamination on the permeability of a sample already characterised by a low-permeability host-rock will be small. More porous sandstones therefore have the potential to be more anisotropic when the permeability anisotropy is the result of low-permeability laminations, which is what we see in our data (Figs. 9, 10a). As noted above, when the permeability anisotropy is the result of a pore shape preferred orientation, rather than low-permeability laminations, high-porosity sandstone can be characterised by mild permeability anisotropies (as can be seen for published data for sandstone with a porosity > 20%; Fig. 12a).

#### **P-wave velocity anisotropy**

P-wave velocity ratio is plotted as a function of porosity in Fig. 12b, together with previously published data for Buntsandstein sandstones from EPS-1 (Heap et al. 2017). Our *P*-wave velocity ratios are in agreement with the previously published data (Fig. 12b). The *P*-wave velocity ratios from our study range from 0.85 to 0.88, compared to from 0.89 to 0.97 for the data from Heap et al. (2017). Therefore, for all the data, the *P*-wave velocity is faster parallel to bedding. We also note that the *P*-wave velocity ratio for the data from Heap et al. (2017) does not vary as a function of porosity, in accordance with our new data. A slower *P*-wave velocity perpendicular to bedding compared to parallel to bedding can be explained by the higher number of grain-to-grain contacts typically encountered by elastic waves travelling perpendicular to bedding. Grains in sedimentary rocks are often oblate in shape and settle such that their long-axis is perpendicular to bedding. As a result, an elastic wave travelling perpendicular to bedding will encounter more grain-to-grain contacts, which will attenuate and slow the wave, than a wave travelling parallel to bedding. This explains why our samples are characterised by a *P*-wave velocity anisotropy. A *P*-wave anisotropy of about 0.8 has been previously observed in laboratory studies on sandstones (Benson et al. 2005; Louis et al. 2008; Menezes and Lempp 2018).

#### **Implications for geothermal reservoirs**

An understanding of large-scale fluid flow is important for the optimisation of geothermal resources. Indeed, there are many modelling studies that have modelled fluid flow and convection in geothermal reservoirs (Guillou-Frottier et al. 2013; Magnenet et al. 2014; Vallier et al. 2018, 2019; Duwiquet et al. 2019, 2021). These studies, which often assume a permeability isotropy within the different layers in the model, highlight that large-scale hydrothermal convection, and the patterns of convection, can be influenced by a change in permeability of an order of magnitude. However, our new data suggest that permeability anisotropy in reservoir sandstones can be on the order of up to four orders of magnitude. Therefore, we recommend that future fluid flow modelling studies

designed to better understand hydrothermal circulation at the geothermal sites within the Upper Rhine Graben should consider incorporating a permeability anisotropy for the Buntsandstein sandstone in their models. We also recommend that the presence of a permeability anisotropy in sandstone should be considered when modelling hydrothermal circulation at sandstone reservoirs worldwide, especially if the reservoir sandstones contain obvious bedding/laminations. Our data also show that permeability anisotropy in the Buntsandstein sandstone can be greater in more porous rocks and, therefore, if fluid flow models for the Upper Rhine Graben separate the Buntsandstein sandstone into several units, higher permeability anisotropies should perhaps be considered for the higher porosity sections of the Buntsandstein. We also recommend that models designed to better understand hydrothermal circulation at sandstone reservoirs worldwide should consider higher permeability anisotropies for high-porosity sandstones that contain obvious bedding/laminations.

Finally, we highlight that our laboratory data represent the permeability anisotropy of the “matrix” rock (i.e. excluding large-scale fractures) and, as a result, require upscaling before they can be used in large-scale modelling (Kushnir et al. 2018b). Although we note that the fracture density in the granitic reservoir at Soultz-sous-Forêts (and other geothermal sites in the Upper Rhine Graben) is much higher than that in the Buntsandstein (Heap et al. 2019a, b), fractures are still considered to play an important role in dictating the permeability of the Buntsandstein (Kushnir et al. 2018b). Nevertheless, the analysis of Kushnir et al. (2018b) also shows that the matrix permeability can still influence upscaled permeability values for the Buntsandstein, and this will be especially true where fractures have been sealed by mineral precipitation (Griffiths et al. 2016; McNamara et al. 2016). Therefore, although the values we provide here are matrix permeabilities, we suggest that the large matrix permeability anisotropies measured (up to four orders of magnitude) are capable of impacting regional fluid-flow and should still be considered in large-scale permeability modelling alongside other sources of permeability such as fracture preferred orientations.

Our data also show that the sandstones of the Buntsandstein can also be characterised by a P-wave anisotropy, which we suggest could also be considered in studies designed to, for example, locate and analyse microseismicity during production and simulation (Cuenot et al. 2008; Dorbath et al. 2009; Lengliné et al. 2017; Cauchie et al. 2020), construct 3D models and detailed images of geothermal reservoirs (Calò et al. 2013; Lehujeur et al. 2018), and for the analysis of induced and triggered seismicity (Schmittbuhl et al. 2021).

## Conclusions

We assessed the permeability anisotropy of reservoir sandstones from a geothermal reservoir with visible laminations. Laboratory permeability measurements showed that laminations associated with bedding can create a permeability anisotropy of up to four orders of magnitude (much higher than permeability anisotropies typically reported for sandstones resulting from bedding). For all the samples studied herein, permeability parallel to bedding was higher than permeability perpendicular to bedding. Combining quantitative microstructural analyses and a permeability model for polydisperse granular media, we showed that the measured permeability anisotropy was the result of thin,

low-permeability laminations. Our data also showed that more porous sandstones are characterised by larger permeability anisotropies, explained by the fact that the permeability of a sample with a higher host-rock permeability will be more impacted by the presence of a low-permeability layer. We conclude by suggesting that permeability anisotropy should be considered when modelling fluid flow within sandstone geothermal reservoirs, and that this consideration may be particularly important when dealing with high-porosity sandstone reservoirs that could be characterised by significant permeability anisotropies.

#### Acknowledgements

We thank Bertrand Renaudie, Alexandra Kushnir, Lucille Carbillet, Emma Vairé, Florian Zapata, Estelle Neyrinck, and Fabian Wadsworth. The comments of two anonymous reviewers helped improve this manuscript.

#### Author contributions

MJH designed the study. MG measured and analysed the data, prepared the figures, and wrote the first draft of the manuscript. MJH and PB helped interpret the data, and contributed to the writing of the manuscript. All authors read and approved the final manuscript.

#### Funding

This work of the Interdisciplinary Thematic Institute GeoT, as part of the ITI 2021–2028 program of the University of Strasbourg, CNRS and Inserm, was supported by IdEx Unistra (ANR-10-IDEX-0002), and by SFRI-STRAT'US project (ANR ANR-20-SFRI-001) under the framework of the French Investments for the Future Program. M.J. Heap acknowledges support from the Institut Universitaire de France (IUF).

#### Availability of data and materials

All the data collected for this study can be found in Table 1.

#### Declarations

##### Competing interests

The authors declare no competing interests.

Received: 15 September 2022 Accepted: 19 December 2022

Published online: 30 December 2022

#### References

- Aichholzer C, Düringer P, Orciani S, Genter A. New stratigraphic interpretation of the Soultz-sous-Forêts 30-year-old geothermal wells calibrated on the recent one from Rittershoffen (upper Rhine Graben, France). *Geotherm Energy*. 2016;4(1):1–26.
- Aichholzer C, Düringer P, Genter A. Detailed descriptions of the lower-middle triassic and permian formations using cores and gamma-rays from the EPS-1 exploration geothermal borehole (Soultz-sous-Forêts, Upper Rhine Graben, France). *Geotherm Energy*. 2019;7(1):1–28.
- Baillieux P, Schill E, Edel JB, Mauri G. Localization of temperature anomalies in the Upper Rhine Graben: insights from geophysics and neotectonic activity. *Int Geol Rev*. 2013;55(14):1744–62.
- Baud P, Louis L, David C, Rawling GC, Wong TF. Effects of bedding and foliation on mechanical anisotropy, damage evolution and failure mode. *Geol Soc London Spec Publ*. 2005;245(1):223–49.
- Baud P, Meredith P, Townend E. Permeability evolution during triaxial compaction of an anisotropic porous sandstone. *J Geophys Res Solid Earth*. 2012;117(B5):B05203. <https://doi.org/10.1029/2012JB009176>.
- Benson PM, Meredith PG, Platzman ES. Relating pore fabric geometry to acoustic and permeability anisotropy in Crab Orchard Sandstone: a laboratory study using magnetic ferrofluid. *Geophys Res Lett*. 2003;30(19):1976. <https://doi.org/10.1029/2003GL017929>.
- Benson PM, Meredith PG, Platzman ES, White RE. Pore fabric shape anisotropy in porous sandstones and its relation to elastic wave velocity and permeability anisotropy under hydrostatic pressure. *Int J Rock Mech Min Sci*. 2005;42(7–8):890–9.
- Bourbie T, Zinszner B. Hydraulic and acoustic properties as a function of porosity in Fontainebleau sandstone. *J Geophys Res Solid Earth*. 1985;90(B13):11524–32.
- Brace W, Walsh JB, Frangos WT. Permeability of granite under high pressure. *J Geophys Res*. 1968;73(6):2225–36.
- Calò M, Kinnaert X, Dorbath C. Procedure to construct three-dimensional models of geothermal areas using seismic noise cross-correlations: application to the Soultz-sous-Forêts enhanced geothermal site. *Geophys J Int*. 2013;194(3):1893–9.
- Cauchie L, Lengliné O, Schmittbuhl J. Seismic asperity size evolution during fluid injection: case study of the 1993 Soultz-sous-Forêts injection. *Geophys J Int*. 2020;221(2):968–80.
- Chang C, Zoback MD, Khaksar A. Empirical relations between rock strength and physical properties in sedimentary rocks. *J Petrol Sci Eng*. 2006;51(3–4):223–37.

- Clavaud JB, Maineult A, Zamora M, Rasolofosaon P, Schlitter C. Permeability anisotropy and its relations with porous medium structure. *J Geophys Res Solid Earth* 2008;113:B01202. <https://doi.org/10.1029/2007JB005004>.
- Cuenot N, Dorbath C, Dorbath L. Analysis of the microseismicity induced by fluid injections at the EGS site of Soultz-sous-Forêts (Alsace, France): implications for the characterization of the geothermal reservoir properties. *Pure Appl Geophys*. 2008;165(5):797–828.
- Dautriat J, Gland N, Guelard J, Dimanov A, Raphanel JL. Axial and radial permeability evolutions of compressed sandstones: end effects and shear-band induced permeability anisotropy. *Pure Appl Geophys*. 2009;166(5):1037–61.
- Dezayes C, Genter A, Valley B. Structure of the low permeable naturally fractured geothermal reservoir at Soultz. *CR Geosci*. 2010;342(7–8):517–30.
- Dezayes C, Lerouge C, Innocent C, Lach P. Structural control on fluid circulation in a graben system: constraints from the Saint Pierre Bois quarry (Vosges, France). *J Struct Geol*. 2021;146: 104323.
- Dorbath L, Cuenot N, Genter A, Frogneux M. Seismic response of the fractured and faulted granite of Soultz-sous-Forêts (France) to 5 km deep massive water injections. *Geophys J Int*. 2009;177(2):653–75.
- Düringer P, Aichholzer C, Orciani S, Genter A. The complete lithostratigraphic section of the geothermal wells in Rittershoffen (Upper Rhine Graben, eastern France): a key for future geothermal wells. *BSGF-Earth Sci Bull*. 2019;190(1):13.
- Duwiquet H, Arbaret L, Guillou-Frottier L, Heap MJ, Bellanger M. On the geothermal potential of crustal fault zones: a case study from the Pontgibaud area (French Massif Central, France). *Geotherm Energy*. 2019;7(1):1–29.
- Duwiquet H, Guillou-Frottier L, Arbaret L, Bellanger M, Guillon T, Heap MJ. Crustal fault zones (CFZ) as geothermal power systems a preliminary 3d thm model constrained by a multidisciplinary approach. *Geofluids*. 2021;2021:8855632. <https://doi.org/10.1155/2021/8855632>.
- Eberhart-Phillips D, Han DH, Zoback MD. Empirical relationships among seismic velocity, effective pressure, porosity, and clay content in sandstone. *Geophysics*. 1989;54(1):82–9.
- Ehrenberg SN, Nadeau PH. Sandstone vs carbonate petroleum reservoirs a global perspective on porosity depth and porosity permeability relationships. *AAPG Bull*. 2005;89(4):435–45.
- Farquharson JI, Heap MJ, Lavallée Y, Varley NR, Baud P. Evidence for the development of permeability anisotropy in lava domes and volcanic conduits. *J Volcanol Geoth Res*. 2016;323:163–85.
- Farrell NJC, Healy D. Anisotropic pore fabrics in faulted porous sandstones. *J Struct Geol*. 2017;104:125–41.
- Farrell NJC, Healy D, Taylor CW. Anisotropy of permeability in faulted porous sandstones. *J Struct Geol*. 2014;63:50–67.
- Farrell NJC, Debenham N, Wilson L, Wilson MJ, Healy D, King RC, Taylor CW. The effect of authigenic clays on fault zone permeability. *J Geophys Res Solid Earth*. 2021;126(10):e2021JB022615.
- Gehne S, Benson PM. Permeability and permeability anisotropy in crab orchard sandstone: experimental insights into spatio-temporal effects. *Tectonophysics*. 2017;712:589–99.
- Genter A, Traineau H. Analysis of macroscopic fractures in granite in the HDR geothermal well EPS-1, Soultz-sous-Forêts, France. *J Volcanol Geoth Res*. 1996;72(1–2):121–41.
- Glaas C, Vidal J, Genter A. Structural characterization of naturally fractured geothermal reservoirs in the central Upper Rhine Graben. *J Struct Geol*. 2021;148: 104370.
- Griffiths L, Heap MJ, Wang F, Daval D, Gilg HA, Baud P, Genter A. Geothermal implications for fracture-filling hydrothermal precipitation. *Geothermics*. 2016;64:235–45.
- Guéguen Y, Palciauskas V. Introduction to the physics of rocks. Princeton University Press; 1994.
- Guillou-Frottier L, Carré C, Bourguin B, Bouchot V, Genter A. Structure of hydrothermal convection in the Upper Rhine Graben as inferred from corrected temperature data and basin-scale numerical models. *J Volcanol Geoth Res*. 2013;256:29–49.
- Haffen S, Géraud Y, Diraison M, Dezayes C. Determination of fluid-flow zones in a geothermal sandstone reservoir using thermal conductivity and temperature logs. *Geothermics*. 2013;46:32–41.
- Han DH, Nur A, Morgan D. Effects of porosity and clay content on wave velocities in sandstones. *Geophysics*. 1986;51(11):2093–107.
- Harlé P, Kushnir AR, Aichholzer C, Heap MJ, Hehn R, Maurer V, Düringer P. Heat flow density estimates in the upper Rhine Graben using laboratory measurements of thermal conductivity on sedimentary rocks. *Geotherm Energy*. 2019;7(1):1–36.
- Heap MJ. The influence of sample geometry on the permeability of a porous sandstone. *Geosci Instrum Methods Data Syst*. 2019;8(1):55–61.
- Heap MJ, Kennedy BM. Exploring the scale-dependent permeability of fractured andesite. *Earth Planet Sci Lett*. 2016;447:139–50.
- Heap MJ, Lavallée Y, Petrakova L, Baud P, Reuschlé T, Varley NR, Dingwell DB. Microstructural controls on the physical and mechanical properties of edifice-forming andesites at Volcán de Colima, Mexico. *J Geophys Res Solid Earth*. 2014;119(4):2925–63.
- Heap MJ, Kushnir AR, Gilg HA, Wadsworth FB, Reuschlé T, Baud P. Microstructural and petrophysical properties of the Permo-Triassic sandstones (Buntsandstein) from the Soultz-sous-Forêts geothermal site (France). *Geotherm Energy*. 2017;5(1):1–37.
- Heap MJ, Reuschlé T, Kushnir AR, Baud P. The influence of hydrothermal brine on the short-term strength and elastic modulus of sandstones from exploration well EPS-1 at Soultz-sous-Forêts (France). *Geotherm Energy*. 2018;6(1):1–22.
- Heap MJ, Villeneuve M, Kushnir AR, Farquharson JI, Baud P, Reuschlé T. Rock mass strength and elastic modulus of the Buntsandstein: an important lithostratigraphic unit for geothermal exploitation in the upper Rhine Graben. *Geothermics*. 2019a;77:236–56.
- Heap MJ, Kushnir AR, Gilg HA, Violay ME, Harlé P, Baud P. Petrophysical properties of the Muschelkalk from the Soultz-sous-Forêts geothermal site (France), an important lithostratigraphic unit for geothermal exploitation in the Upper Rhine Graben. *Geotherm Energy*. 2019b;7(1):1–29.
- Heap MJ, Gravley DM, Kennedy BM, Gilg HA, Bertolett E, Barker SL. Quantifying the role of hydrothermal alteration in creating geothermal and epithermal mineral resources: the Ohakuri ignimbrite (Taupō Volcanic Zone, New Zealand). *J Volcanol Geoth Res*. 2020;390: 106703.

- Hicks TW, Pine RJ, Willis-Richards J, Xu S, Jupe AJ, Rodrigues NEV. A hydro-thermo-mechanical numerical model for HDR geothermal reservoir evaluation. *Int J Rock Mech Mining Sci Geomechan Abstr.* 1996;33(5):499–511.
- Hill S, Villeneuve MC, McNamara D. Physical and mechanical characteristic relationships of late-cretaceous to eocene reservoir rocks in the Maui, Maari and Manaia fields, New Zealand. *J Petrol Sci Eng.* 2022;213: 110375.
- Huenges E, Ledru P. Geothermal energy systems: exploration development, and utilization. Hoboken: John Wiley Sons; 2011.
- Kim KY, Zhuang L, Yang H, Kim H, Min KB. Strength anisotropy of Berea sandstone: results of X-ray computed tomography, compression tests, and discrete modeling. *Rock Mech Rock Eng.* 2016;49(4):1201–10.
- Kushnir AR, Heap MJ, Baud P, Gilg HA, Reuschlé T, Lerouge C, Düringer P. Characterizing the physical properties of rocks from the paleozoic to permo-triassic transition in the upper Rhine Graben. *Geotherm Energy.* 2018a;6(1):1–32.
- Kushnir AR, Heap MJ, Baud P. Assessing the role of fractures on the permeability of the Permo-Triassic sandstones at the Soultz-sous-Forêts (France) geothermal site. *Geothermics.* 2018b;74:181–9.
- Ledéseret B, Hebert R, Genter A, Bartier D, Clauer N, Grall C. Fractures, hydrothermal alterations and permeability in the soultz enhanced geothermal system. *CR Geosci.* 2010;342(7–8):607–15.
- Lehujeur M, Vergne J, Schmittbuhl J, Le ZigoneChenadec DA, EstOF, Team. Reservoir imaging using ambient noise correlation from a dense seismic network. *J Geophys Res Solid Earth.* 2018;123(8):6671–86.
- Lengliné O, Boubacar M, Schmittbuhl J. Seismicity related to the hydraulic stimulation of GRT1, Rittershoffen. *Fr Geophys J Int.* 2017;208(3):1704–15.
- Louis L, David C, Metz V, Robion P, Menendez B, Kissel C. Microstructural control on the anisotropy of elastic and transport properties in undeformed sandstones. *Int J Rock Mech Min Sci.* 2005;42(7–8):911–23.
- Louis L, Chen TMN, David C, Robion P, Wong TF, Song SR. Anisotropy of magnetic susceptibility and P-wave velocity in core samples from the Taiwan Chelungpu-fault drilling project (TCDF). *J Struct Geol.* 2008;30(8):948–62.
- Louis L, Baud P, Wong TF. Microstructural inhomogeneity and mechanical anisotropy associated with bedding in Rothbach sandstone. *Pure Appl Geophys.* 2009;166(5):1063–87.
- Magnenet V, Fond C, Genter A, Schmittbuhl J. Two-dimensional THM modelling of the large scale natural hydrothermal circulation at Soultz-sous-Forêts. *Geotherm Energy.* 2014;2(1):1–21.
- Martys NS, Torquato S, Bentz DP. Universal scaling of fluid permeability for sphere packings. *Phys Rev E.* 1994;50(1):403.
- Masch FD, Denny KJ. Grain size distribution and its effect on the permeability of unconsolidated sands. *Water Resour Res.* 1966;2(4):665–77.
- McNamara DD, Lister A, Prior DJ. Calcite sealing in a fractured geothermal reservoir insights from combined EBSD and chemistry mapping. *J Volcanol Geoth Res.* 2016;323:38–52.
- Menezes FF, Lempp C. On the structural anisotropy of physical and mechanical properties of a Bunter Sandstone. *J Struct Geol.* 2018;114:196–205.
- Meng F, Li X, Baud P, Wong TF. Bedding anisotropy and effective stress law for the permeability and deformation of clayey sandstones. *Rock Mech Rock Eng.* 2021;54(10):5167–84.
- Nelson, P. H. Permeability-porosity relationships in sedimentary rocks. *Log Anal.* 1994 35(03).
- Pribnow D, Schellschmidt R. Thermal tracking of upper crustal fluid flow in the Rhine Graben. *Geophys Res Lett.* 2000;27(13):1957–60.
- Schmittbuhl J, Lambotte S, Lengliné O, Grunberg M, Jund H, Vergne J, et al. Induced and triggered seismicity below the city of Strasbourg, France from November 2019 to January 2021. *Comptes Rendus Géoscience.* 2021;353(5):1–24.
- Shepherd RG. Correlations of permeability and grain size. *Groundwater.* 1989;27(5):633–8.
- Shipton ZK, Evans JP, Robeson KR, Forster CB, Snelgrove S. Structural heterogeneity and permeability in faulted eolian sandstone: Implications for subsurface modeling of faults. *AAPG Bull.* 2002;86(5):863–83.
- Vallier B, Magnenet V, Schmittbuhl J, Fond C. THM modeling of hydrothermal circulation at Rittershoffen geothermal site. *France Geotherm Energy.* 2018;6(1):1–26.
- Vallier B, Magnenet V, Schmittbuhl J, Fond C. Large scale hydro-thermal circulation in the deep geothermal reservoir of Soultz-sous-Forêts (France). *Geothermics.* 2019;78:154–69.
- Vasseur J, Wadsworth FB, Lavallée Y, Dingwell DB. Dynamic elastic moduli during isotropic densification of initially granular media. *Geophys J Int.* 2016;204(3):1721–8.
- Vidal J, Genter A. Overview of naturally permeable fractured reservoirs in the central and southern upper Rhine Graben: Insights from geothermal wells. *Geothermics.* 2018;74:57–73.
- Vidal J, Genter A, Schmittbuhl J. How do permeable fractures in the triassic sediments of Northern Alsace characterize the top of hydrothermal convective cells? Evidence from Soultz geothermal boreholes (France). *Geotherm Energy.* 2015;3(1):1–28.
- Villeneuve MC, Heap MJ, Kushnir AR, Qin T, Baud P, Zhou G, Xu T. Estimating in situ rock mass strength and elastic modulus of granite from the Soultz-sous-Forêts geothermal reservoir (France). *Geotherm Energy.* 2018;6(1):1–29.
- Wadsworth FB, Vasseur J, Scheu B, Kendrick JE, Lavallée Y, Dingwell DB. Universal scaling of fluid permeability during volcanic welding and sediment diagenesis. *Geology.* 2016;44(3):219–22.
- Zhu W, Wong TF. The transition from brittle faulting to cataclastic flow: permeability evolution. *J Geophys Res Solid Earth.* 1997;102(B2):3027–41.

## Publisher's Note

Springer Nature remains neutral with regard to jurisdictional claims in published maps and institutional affiliations.